



Deposited via The University of Leeds.

White Rose Research Online URL for this paper:

<https://eprints.whiterose.ac.uk/id/eprint/210188/>

Version: Preprint

---

**Preprint:**

Livermore, P., de Ridder, S., Wu, L. et al. (2024) Reconstructions of Jupiter's magnetic field using physics informed neural networks. [Preprint]

---

**Reuse**

Items deposited in White Rose Research Online are protected by copyright, with all rights reserved unless indicated otherwise. They may be downloaded and/or printed for private study, or other acts as permitted by national copyright laws. The publisher or other rights holders may allow further reproduction and re-use of the full text version. This is indicated by the licence information on the White Rose Research Online record for the item.

**Takedown**

If you consider content in White Rose Research Online to be in breach of UK law, please notify us by emailing [eprints@whiterose.ac.uk](mailto:eprints@whiterose.ac.uk) including the URL of the record and the reason for the withdrawal request.

1  
2  
3  
4  
5  
6  
7  
8  
9  
10  
11  
12  
13  
14  
15  
16  
17  
18

# Reconstructions of Jupiter’s magnetic field using physics informed neural networks

Philip W. Livermore<sup>1</sup>, Leyuan Wu<sup>2</sup>, Longwei Chen<sup>3</sup>, Sjoerd de Ridder<sup>1</sup>

<sup>1</sup>School of Earth and Environment, University of Leeds, Leeds, LS2 9JT  
<sup>2</sup>Key Laboratory of Quantum Precision Measurement of Zhejiang Province, Center for Optics and Optoelectronics Research (COOR), Center for Optics and Optoelectronics Research (COOR), Collaborative Innovation Center for Information Technology in Biological and Medical Physics, College of Science, Zhejiang University of Technology, Hangzhou, 310023, China.  
<sup>3</sup>Guangxi Key Laboratory of Exploration For Hidden Metallic Ore Deposits, College of Earth Sciences, Guilin University of Technology, Guilin, 541006, China.

## Key Points:

- We present two reconstructions of Jupiter’s magnetic field using physics informed neural networks: PINN33, based on the first 33 orbits and PINN50, based on the first 50 orbits.
- Compared with spherical harmonic based methods, our reconstructions give a more stable downwards continuation and result in clearer images at depth of Jupiter’s internal magnetic field
- Our models infer a dynamo at a fractional radius of 0.8.

---

Corresponding author: Phil Livermore, [p.w.livermore@leeds.ac.uk](mailto:p.w.livermore@leeds.ac.uk)

## Abstract

Magnetic sounding using data collected from the Juno mission can be used to provide constraints on Jupiter’s interior. However, inwards continuation of reconstructions assuming zero electrical conductivity and a representation in spherical harmonics are limited by the enhancement of noise at small scales. In this paper we describe new reconstructions of Jupiter’s internal magnetic field based on physics-informed neural networks and either the first 33 (PINN33) or the first 50 (PINN50) of Juno’s orbits. The method can resolve local structures, and allows for weak ambient electrical currents. Compared with other methods, our reconstructions of Jupiter’s magnetic field both on and above the surface are similar, and we achieve a similar fit to the Juno data. However, our models are not hampered by noise at depth, and so offer a much clearer picture of the interior structure. We estimate that the dynamo boundary is at a fractional radius of 0.8. At this depth, the magnetic field is arranged into longitudinal bands, and the great blue spot appears to be rooted in neighbouring structures of oppositely signed flux.

## Plain Language Summary

A major goal of the Juno mission is to better constrain the interior structure of Jupiter. One method of doing this is to reconstruct Jupiter’s magnetic field using measurements from Juno, which can then be used to probe the interior. One particular internal region of interest is the dynamo, within which the planetary magnetic field is generated. Standard assumptions of zero electrical conductivity and global solutions allow the reconstructions to be inwards extrapolated, however this method of imaging is limited by amplified noise. Here, we present reconstructions based on recent advances in machine learning, in which the physical assumptions are relaxed and we allow for local structures. Our method shows a much clearer image of Jupiter’s interior than has been possible before.

## 1 Introduction

The Juno mission, launched in 2011 (Bolton et al., 2010), has revolutionised our understanding of Jupiter’s interior through the collection of both gravity and magnetic measurements in orbit since 2016. These new data have not only allowed new constraints on the density structure and zonal flow in the outermost parts of the planet (Kaspi et al., 2018), but have permitted new reconstructions of the magnetic field to unprecedented resolution (e.g. Connerney et al., 2017, 2022). These magnetic maps highlight local features such as the Great Blue Spot, sited within a largescale hemispheric field (Moore et al., 2018) which shows evidence of secular variation (Ridley & Holme, 2016; Moore et al., 2019; Sharan et al., 2022; Bloxham et al., 2022; Connerney et al., 2022).

In order to infer the structure of Jupiter’s internally generated magnetic field, global reconstructions are needed that fit a physical model of the magnetic field to the sparse magnetic dataset collected on orbital trajectories. The physical model commonly adopted is that the measured values come from a region free from electrical currents, and comprise signals dominated by the internally generated field with more minor contributions from an external magnetic field and unmodelled instrumentation noise. Typical studies then proceed by subtracting an approximation to the external field assuming a magnetodisk structure, with estimates of the parameters (Connerney et al., 1981, 2022), although the difficulty in adopting an accurate representation is compounded by its unknown likely time-dependence (Ridley & Holme, 2016; Moore et al., 2019). The remaining signal is then fit in a least-squares sense to an analytic description of an internally-generated magnetic field  $\mathbf{B}$  using a potential  $V$ , with  $\mathbf{B} = -\nabla V$ , which by construction exactly satisfies  $\mathbf{J} = \mathbf{0}$  where  $\mathbf{J}$  is the ambient electrical current. The potential is then typically represented in terms of a truncated spherical harmonic expansion (Connerney, 1981), similar to comparable studies for Earth’s magnetic field (e.g. Alken et al., 2021).

Such reconstructions allow not only spatial interpolation between the Juno measurements, but also extrapolation into regions unconstrained by measurements. Downwards continuation radially inwards under Jupiter’s surface, assuming the same electrically-insulating physics, is of particular interest because it allows inference of the dynamo radius, typical values for which are  $0.8 - 0.83R_J$ , where  $R_J$  is Jupiter’s equatorial radius (71,492km) (Connerney et al., 2022; Sharan et al., 2022). However, this downwards continuation is numerically unstable because errors in small-scales, caused by leakage from unmodelled signals, become amplified more rapidly with decreasing radius than errors in large-scales, eventually producing a signal swamped with noise.

In this paper, we propose a novel representation of Jupiter’s internal magnetic field based on physics informed neural networks (PINNs). Compared to standard approaches, our models give a similar reconstruction on and above Jupiter’s surface but appear to be more stable under downwards continuation. In the following sections, we first describe the data before outlining our PINN approach. We present some reconstructions and estimates of the dynamo radius, which we compare with those from existing methods, and end with a brief discussion.

## 2 Data

Our work is based the vector magnetic field measured by Juno within the first 50 perijoves during the period 2016 to 2023, which contains the prime mission of 33 orbits. From these data we excluded the second perijove (PJ2) due to a spacecraft safe mode entry Connerney et al. (2018). The original observations were down-sampled to 30 s sampling rate (this being the approximate rotation time of the spacecraft) using a mean-value filter. In order to maximise the internal signal content of the data, we used only measurements recorded at planetocentric spherical radius  $r \leq 4.0R_J$  (where  $R_J = 71,492$  km, the equatorial radius). In total, there were 28011 3-component measurements of the magnetic field, of periapsis  $1.02 R_J$  and taking magnitudes in the range of approximately 0.065 – 16 Gauss. Figure 1 shows an overview of the data used in this work.

## 3 Method

Physics informed neural networks, or PINNs, offer a technique for representing spatially dependent quantities by a neural network that are constrained not only by data but also physical laws (Raissi et al., 2019). There are two key differences between a PINN representation and existing reconstructions based on a spherical-harmonic potential. First, existing methods fit data in a weak sense (by least squares) to physics imposed in a strong form (by assuming an internal potential field representation). This is quite different in a PINN, where both data and physics are fit in a weak form, which makes them particularly effective in problems when the data and physics are imperfectly known (Karniadakis et al., 2021), as for Jupiter. Instead of assuming that  $\mathbf{J} = 0$  and seeking a fit to an internally-generated magnetic solution, instead we minimise the root-mean-squared electrical current  $\mathbf{J}$  which allows, for example, weak nonzero electric currents if the data require them. Another key distinction is that we don’t (and indeed cannot) separate internal and external fields as we fit the PINN to the fundamental physical law, rather than to an analytic solution which assumes the location of source.

A second important difference is in the spatial representation. A spherical harmonic representation, an analytic solution to Laplace’s equation, is defined by a set of Gauss coefficients, whose globally resolved wavelength is approximately  $2\pi/(N+1/2)$ , where  $N$  is the maximum degree  $N$  (Backus et al., 1996). In contrast, a neural network is a meshless method that can define both local and global solutions. It is defined by a set of weights and biases that describe the internal coefficients of connected neurons, arranged in a structure that is governed by various hyperparameters: the number of neurons per layer, the number of layers, and the activation function.

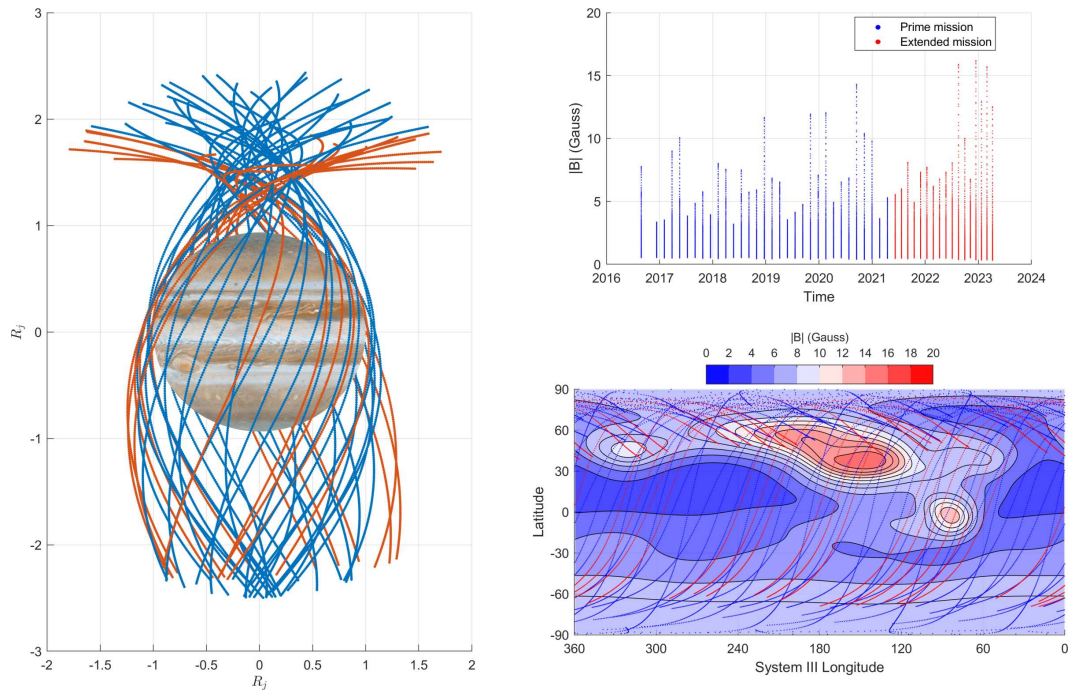


**Figure 1.** Juno data used in this work. Left: Juno’s global coverage after 50 orbits, showing Juno’s trajectory within radius  $2.5 R_J$ ; the colours show the 33 prime mission orbits (red lines) and extended mission (blue lines). Upper right: time span and magnitude range per orbit of Juno magnetic data. Lower right: orbital position (radius within  $4.0 R_J$ ) projected onto a background contour map of the magnitude of magnetic field at  $r = R_J$  reconstructed using model PINN50e.

119 We work in a planetocentric Cartesian coordinate system, and write the magnetic  
 120 field in terms of a vector-potential:  $\mathbf{B} = \nabla \times \mathbf{A}$ , which satisfies the fundamental rela-  
 121 tion  $\nabla \cdot \mathbf{B} = 0$ . The three independent components of  $\mathbf{A}$ ,  $(A_x, A_y, A_z)$ , are expressed  
 122 as individual feed-forward neural networks (FNNs) with 6 hidden layers, 40 neurons per  
 123 layer and swish activation functions. We rescale the input  $\mathbf{r} = (x, y, z)$  coordinates to  
 124  $[-1, 1]^3$ , but leave the data unscaled as it is handled by an appropriate dynamic weight-  
 125 ing.

126 We denote the set of tunable parameters (weights and biases) of the networks by  
 127  $\Theta$ , and the representation of  $\mathbf{A}$  and  $\mathbf{B}$  as  $\mathbf{A}_\Theta(\mathbf{r})$  and  $\mathbf{B}_\Theta(\mathbf{r})$ . A physics-informed model  
 128 is trained by minimizing the following loss function:

$$129 \quad \mathcal{L}(\Theta) = w_d \mathcal{L}_d(\Theta) + w_p \mathcal{L}_p(\Theta), \quad (1)$$

130 where

$$131 \quad \mathcal{L}_d(\Theta) = \frac{1}{N_d} \sum_i^{N_d} |\mathbf{B}_\Theta(\mathbf{r}_d^i) - \mathbf{B}(\mathbf{r}_d^i)|^2, \quad \mathcal{L}_p(\Theta) = \frac{1}{N_p} \sum_i^{N_p} |(\nabla \times \mathbf{B}_\Theta)(\mathbf{r}_p^i)|^2, \quad (2)$$

132 are the data misfit and physics loss terms with weights  $w_d$  and  $w_p$ ,  $N_p$ ,  $\mathbf{r}_p^i$  are the num-  
 133 ber and location of the collocation points used to constrain the physics loss, and  $N_d$  are  
 134 the number of Juno data used, each of which has location  $\mathbf{r}_d^i$  and vector value  $\mathbf{B}(\mathbf{r}_d^i)$ .  
 135 The contribution to the data loss from each measurement is assumed equal, as is the con-  
 136 tribution to the physics loss from each of the collocation points. The quantities derived  
 137 from  $\mathbf{A}_\Theta$ , namely  $\mathbf{B}_\Theta(\mathbf{r})$  and  $\nabla \times \mathbf{B}_\Theta = \nabla(\nabla \cdot \mathbf{A}_\Theta) - \nabla^2 \mathbf{A}_\Theta$  are computed using au-  
 138 tomatic differentiation (AD) (Baydin et al., 2018). All neural network models are built  
 139 with the machine learning framework TensorFlow (Abadi et al., 2016), and trained with  
 140 the built-in Adam optimizer (Kingma & Ba, 2015) over 12,000 epochs with batch size  
 141 10,000. An empirical learning-rate annealing strategy, with an initial learning rate of 0.002,  
 142 and an exponential decay with a decay rate of 0.8 and a decay step of 1,000 iterations  
 143 are adopted. From a limited number of tests of various network sizes, this network was  
 144 just large enough to fit well all the data and physics constraints. We do not use any ex-  
 145 plicit spatial regularisation in our method.

146 Despite success across a range of applications, the original formulation of Raissi  
 147 et al. (2019) sometimes struggles to converge on an accurate solution; here we apply two  
 148 techniques to improve the method. First, rather than prescribe the weight parameters  
 149  $w_d$  and  $w_p$ , we allow them to be chosen dynamically. We fix  $w_p = 1$ , but allow  $w_d$  to  
 150 change at each training epoch in order to balance the gradients of physical and data-fit  
 151 loss with respect to the model parameters (Wang et al., 2021). Second, we adopt residual-  
 152 based sampling for the physics loss term. While uniformly sampled collocation points  
 153 for the physics term offers a simple approach, recent studies have shown promising im-  
 154 provements in training accuracy by applying nonuniform adaptive sampling strategies  
 155 (Lu et al., 2021; Nabian et al., 2021; Wu et al., 2023). Here we apply a simplified ver-  
 156 sion of the residual-based adaptive distribution (RAD) method described in Wu et al.  
 157 (2023). For the first 3000 epochs we use a uniformly sampled set of points in a fixed re-  
 158 gion, but at epoch 3000 (and every 600 epochs thereafter) we create a pdf, based on sam-  
 159 ples of the physics loss, which we use to resample the collaboration points, effectively in-  
 160 creasing the local weighting in regions with a high physics loss.

161 We create four PINN models, based on either the first 33 (PINN33i, PINN33e) or  
 162 50 Juno orbits (PINN50i, PINN50e), assuming for each that the magnetic field is static.  
 163 We deliberately distinguish between models internal to Jupiter (denoted by the charac-  
 164 ter:i) which downwards continue into  $r \leq R_J$  the data observed in  $r > R_J$ , and those  
 165 external to Jupiter (denoted by the character:e) which interpolate data within the same  
 166 region in which Juno measurements are made  $r > R_J$ . Models PINN50e, PINN33e were  
 167 made first, using 300,000 collocation points within the region  $1 \leq r/R_J \leq 4$ . Models

168 PINN50i and PINN33i were then constructed, using 40,000 collocation points within the  
 169 region  $0.8 \leq r/R_J \leq 1$ ; the data loss term was replaced by a term describing match-  
 170 ing in each component to either PINN50e or PINN33e on  $r = R_J$  at 80,000 randomly  
 171 located points. Although mildly oblate, Jupiter is assumed spherical for simplicity.

## 172 4 Results and discussion

173 Figure 2 shows an orbital comparison of Juno data with four models: PINN33e,  
 174 PINN50e and two recent spherical harmonic models JRM33 ( $N = 18$ ) (Connerney et  
 175 al., 2022) and the Baseline model of Bloxham et al. (2022) with  $N = 32$ . These recent  
 176 models have been chosen because although they are both based on the first 33 orbits,  
 177 they differ in how the spherical harmonics are fitted: JRM33 uses an approach based on  
 178 singular value decomposition, whereas the Baseline model uses regularisation. A sim-  
 179 ple external dipole approximation to the external field (Connerney et al., 2022) has been  
 180 added to the spherical harmonic models, as they only represent the internal field; the PINN  
 181 models represent both internal and external field.

182 The models based only on the prime orbits (1-33, excluding 2): PINN33e, JRM33  
 183 and Baseline show a comparable absolute rms error. For the majority of orbits, PINN33e  
 184 has an error less than JRM33, with a few exceptions such as orbit 32. Over the first 33  
 185 orbits, the rms error for JRM33 is 774.1 nT, compared with 509.3 nT for Baseline and  
 186 511.4 nT for PINN33e. Using these models for orbits 34-50 leads to increasing discrep-  
 187 ancy with the measurements, providing additional evidence for Jupiter’s secular varia-  
 188 tion. Model PINN50e has a slightly higher rms of 589.7 nT for orbits 1-33, but fits the  
 189 data for orbits 34-50 much better because it has been trained in part on these data.

190 The structure of JRM33, Baseline and PINN50i at radii  $r/R_J = 1, 0.95, 0.9, 0.85, 0.8$   
 191 are shown by contours of radial field in figure 3. On  $r = R_J$  the models are almost in-  
 192 distinguishable in terms of physical structure, but as the radius decreases and we (pre-  
 193 sumably) get closer to the dynamo source, the signal strength increases and the length-  
 194 scales decrease. The instability of downwards continuation in the spherical harmonic mod-  
 195 els is readily apparent by the prevalent fine-scaled noise, particularly in the azimuthal  
 196 direction. By comparison, PINN50i remains relatively free of noise and the features at  
 197 depth are much easier to identify.

198 At  $r \leq 0.85R_J$ , the field appears arranged into longitudinal bands, with a strong  
 199 band at high latitude and a weaker band near the equator. Many of the strong patches  
 200 of flux have adjacent oppositely signed counterparts, as can be seen in particular around  
 201 the root of the great blue spot. The hemispheric structure is also striking, with almost  
 202 all the magnetic structure of the field being confined north of the equator.

203 A common approach to determining the dynamo radius is by determining where  
 204 the Lowes-Mauersberger spectrum of the magnetic field (Lowes, 1974; Mauersberger, 1956)  
 205 is flat, which describes a white-noise source. This procedure relies on the spherical har-  
 206 monic representation of the magnetic field:

$$207 \quad \mathbf{B} = -R_J \nabla \sum_{n=0}^N \sum_{m=0}^n \left( \frac{R_J}{r} \right)^{n+1} [g_n^m P_n^m(\theta) \cos(m\phi) + h_n^m P_n^m(\cos\theta) \sin(m\phi)] \quad (3)$$

208 where  $g_n^m$  and  $h_n^m$  are the Gauss coefficients of degree  $n$  and order  $m$  and  $P_n^m$  are asso-  
 209 ciated Legendre functions. The spectrum is then derived as

$$210 \quad R_n = (n+1) \left( \frac{R_J}{r} \right)^{(2n+4)} \sum_{m=0}^n (g_n^m)^2 + (h_n^m)^2 \quad (4)$$

211 In order to find the spectrum for the PINN models, we have two options. First is ana-  
 212 lytic continuation, where we project the field at  $r = R_J$  onto (3) and use the inherent

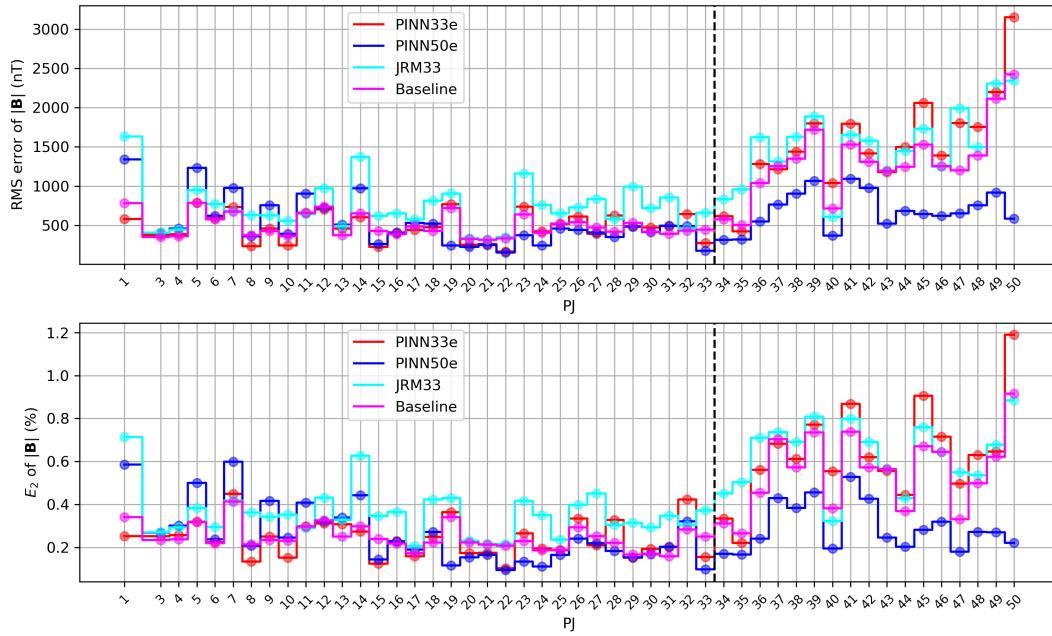


**Figure 2.** Orbital comparison of the discrepancy between various reconstructions of Jupiter’s magnetic field: PINN33e, PINN50e, JRM33 and Baseline, with the Juno data. Taking each orbit in turn, the error is quantified by taking the root mean squared value of the difference in magnitude of the reconstructed magnetic field with the magnitude of each vector measurement. We show the (upper) absolute value of this error, and (lower) relative value of this error compared to the rms observed magnitude over the orbit. The dashed line delineates the prime from the extended mission.

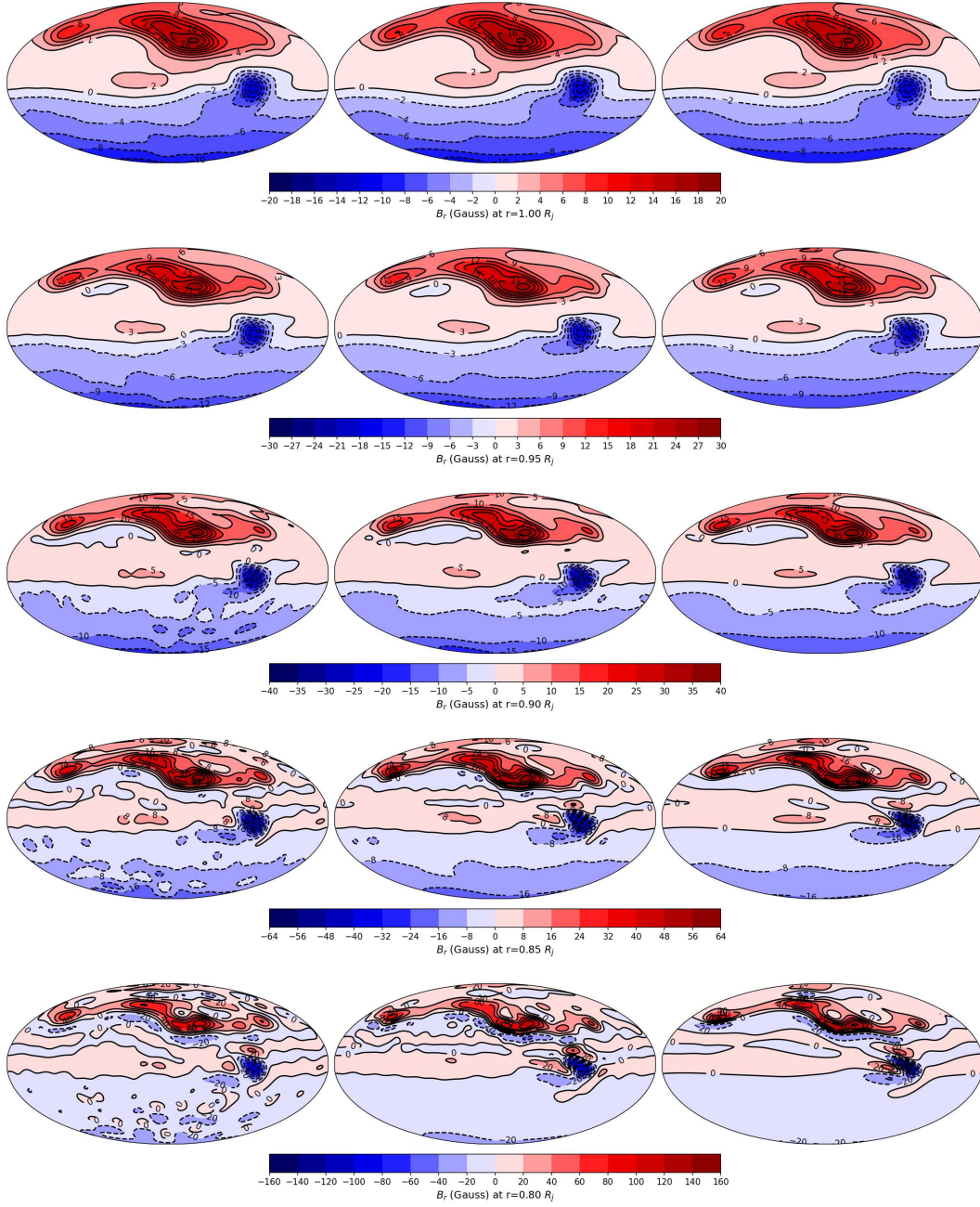


**Figure 3.** The radial component of Jupiter’s magnetic field on various spherical radii inside Jupiter’s surface. The plots are shown on a Mollweide projection with the central meridian at a longitude of  $180^\circ$  west (System III coordinates). Left column shows the JRM33 model ( $N = 18$ ) (Connerney et al., 2022), the middle column shows the Baseline model (Bloxham et al., 2022) ( $N = 32$ ) and the right column shows the PINN model PINN50i.

213 radial dependence within (4). This procedure removes any external field within the PINN  
 214 model. Second, we can use PINN extrapolation, for which we use PINN50i to downwards  
 215 continue, and at each radius  $\tilde{r} < R_J$ , project onto (3) and then use (4) at  $r = \tilde{r}$ . Any  
 216 externally produced field will still be present in the model, albeit at assumed large length-  
 217 scales. In either case, we find the Gauss coefficients by performing a spherical harmonic  
 218 transform of the spherically radial component  $B_r$ .

219 Figure 4 shows the Lowes-Mauersberger spectrum as a function of degree  $n$  for JRM33,  
 220 Baseline and PINN50i (solid lines: analytic continuation, black symbols, PINN extrap-  
 221 olation). At  $r = R_J$  the spectral power for degrees 2–18 agrees well between the mod-  
 222 els and falls off exponentially with  $n$ . The power in the dipole is higher than this sim-  
 223 ple profile predicts. As the radius is decreased the profile flattens as the smaller scales  
 224 become more prominent. Above degree 18, the three analytically continued models di-  
 225 verge, with JRM33 having the most power at high degree. Of the three models, the Base-  
 226 line model (which is the only model with explicit regularisation) has the least power at  
 227 small-degree. For degrees higher than about 18 it is striking that the analytic and PINN  
 228 extrapolation methods diverge, with the PINN extrapolation having smaller power at  
 229 high-degree. These two methods, by construction, agree on  $r = R_J$ , and as the radius  
 230 decreases the discrepancy gets larger.

231 We quantify the slope of the spectrum by fitting a straight line to  $\log_{10} R_n(n)$  for  
 232 degrees 2–18. The lower panel of figure 4 shows the slope variation with radius for four  
 233 models analytically inwards continued using (3). On making the assumption that the  
 234 slope is zero at the source we infer that the dynamo radius is about  $r = 0.8R_J$ , in ap-  
 235 proximate agreement with other studies (Connerney et al., 2022; Sharan et al., 2022).

## 236 5 Concluding remarks

237 We have presented a reconstruction of Jupiter’s magnetic field, based on data from  
 238 Juno within the framework of a physics informed neural network. Our reconstructions  
 239 have a similar misfit to the data compared with other spherical harmonic methods,  
 240 and produce a similar structure of magnetic field on Jupiter’s surface. However, by us-  
 241 ing a meshless method, and only weakly constraining the (poorly known) physics, our  
 242 models are not apparently hostage to the typically enhanced noise with decreasing radi-  
 243 us. Compared with spherical harmonic-based methods, we produce a clearer picture  
 244 at depth of the localised interior magnetic field.

245 The fact that most of the structure in Jupiter’s field appears confined to the north-  
 246 ern hemisphere perhaps makes neural networks a particularly effective modelling tool.  
 247 Even at modest resolution, neural networks are able to very well represent local struc-  
 248 tures, compared to spherical harmonics which are inherently global. More broadly, the  
 249 reduction of noise in the reconstructed field at depth may better constrain secular changes  
 250 close to the dynamo region, which is the subject of a forthcoming study.

## 251 Data Availability Statement

252 The original Juno magnetometer data are publicly available on NASA’s Planetary  
 253 Data System (PDS) at Planetary Plasma Interactions (PPI) node at <https://pds-ppi.igpp.ucla.edu/search/?sc=Juno&t=Jupiter&i=FGM>. The produced PINN models,  
 254 together with input processed Juno data, spherical harmonic models, and all related Python  
 255 code and Jupyter notebook to reproduce all the results in this work, are archived in the  
 256 Github repository [https://github.com/LeyuanWu/JunoMag\\_PINN\\_VP3](https://github.com/LeyuanWu/JunoMag_PINN_VP3).  
 257

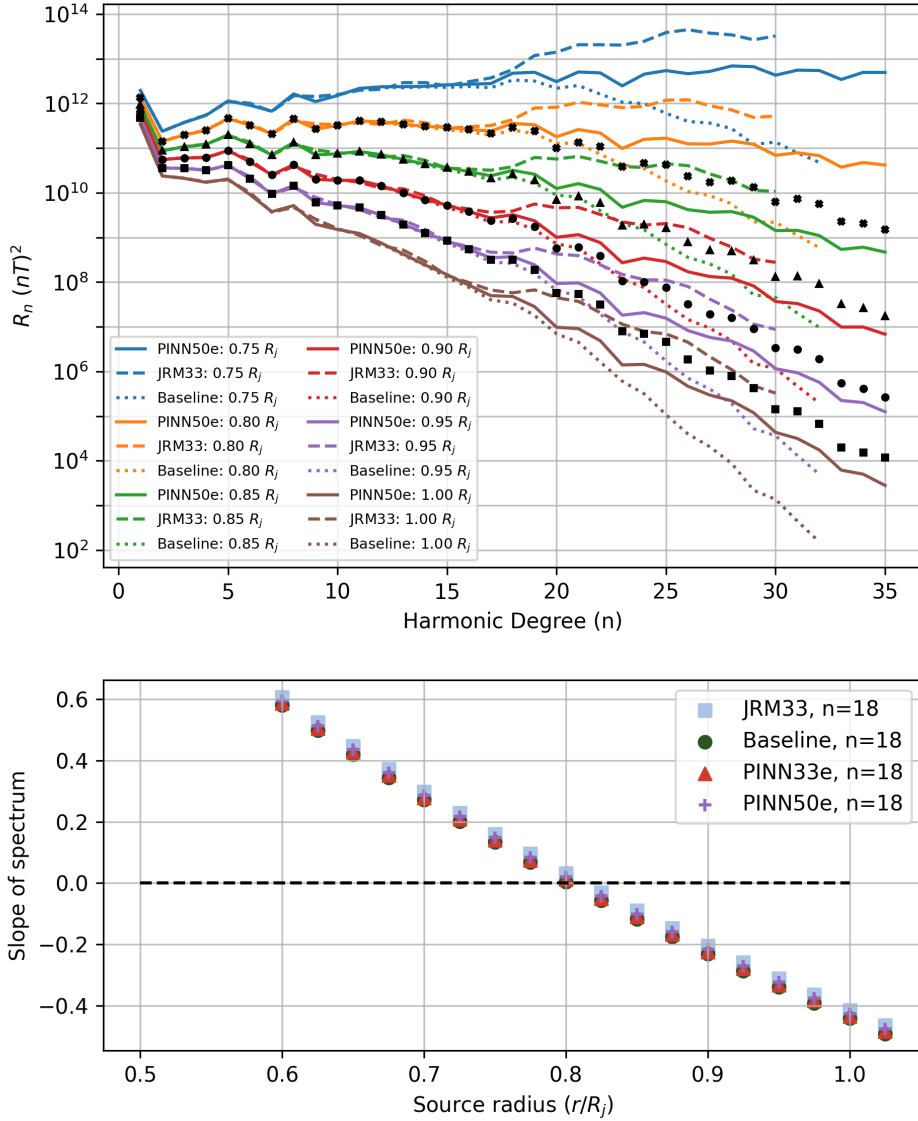


**Figure 4.** Upper panel: Coloured lines show the Lowes-Mauersberger spectrum of three analytically continued models: PINN50e, (to degree  $n = 35$ ), JRM33 (using the full  $n = 30$  resolution) and Baseline ( $n = 32$ ). Black symbols show spectra obtained from PINN extrapolation using PINN50i in  $r < R_J$  (cross:  $0.80R_J$ ; triangle:  $0.85R_J$ ; circle:  $0.90R_J$ ; square:  $0.95R_J$ ). Lower panel: spectral slope with radius assuming analytic continuation, fit to degrees 2–18 for models JRM33, Baseline, PINN33e and PINN50e.

258 **Acknowledgments**

259 This study was funded by the National Natural Science Foundation of China (Grant No.  
260 42374173), National Natural Science Foundation of Guangxi Province of China (Grant  
261 No. 2020GXNSFDA238021). This work was undertaken on ARC4, part of the High Per-  
262 formance Computing facilities at the University of Leeds, UK. We thank Jack Conner-  
263 ney for help with accessing the Juno data.

264

**References**

265

Abadi, M., Barham, P., Chen, J., Chen, Z., Davis, A., Dean, J., . . . Zheng, X.

266

(2016). Tensorflow: a system for large-scale machine learning. In *Proceedings*

267

*of the 12th usenix conference on operating systems design and implementation*

268

(p. 265–283). Savannah, GA, USA: USENIX Association.

269

Alken, P., Thébault, E., Beggan, C. D., Amit, H., Aubert, J., Baerenzung, J., . . .

270

others (2021). International geomagnetic reference field: the thirteenth generation.

271

*Earth, Planets and Space*, *73*(1), 1–25.

272

Backus, G., Parker, R. L., & Constable, C. (1996). *Foundations of geomagnetism*.

273

Cambridge University Press.

274

Baydin, A. G., Pearlmutter, B. A., Radul, A. A., & Siskind, J. M. (2018). Auto-

275

matic differentiation in machine learning: a survey. *Journal of Machine Learning*

276

*Research*, *18*, 153.

277

Bloxham, J., Moore, K. M., Kulowski, L., Cao, H., Yadav, R. K., Stevenson, D. J.,

278

. . . Bolton, S. J. (2022). Differential rotation in jupiter’s interior revealed by

279

simultaneous inversion for the magnetic field and zonal flux velocity. *Journal of*

280

*Geophysical Research: Planets*, *127*(5), e2021JE007138.

281

Bolton, S., Team, J. S., et al. (2010). The juno mission. *Proceedings of the Interna-*

282

*tional Astronomical Union*, *6*(S269), 92–100.

283

Connerney, J. E. P. (1981). The magnetic field of jupiter: A generalized inverse ap-

284

proach. *Journal of Geophysical Research: Space Physics*, *86*(A9), 7679–7693.

285

Connerney, J. E. P., Acuna, M. H., & Ness, N. F. (1981). Modeling the jovian

286

current sheet and inner magnetosphere. *Journal of Geophysical Research: Space*

287

*Physics*, *86*(A10), 8370–8384.

288

Connerney, J. E. P., Benn, M., Bjarno, J. B., Denver, T., Espley, J., Jorgensen,

289

J. L., . . . Smith, E. J. (2017). The juno magnetic field investigation. *Space*

290

*Science Reviews*, *213*(1-4), 39–138. doi: 10.1007/s11214-017-0334-z

291

Connerney, J. E. P., Kotsiaros, S., Oliverson, R. J., Espley, J. R., Joergensen, J. L.,

292

Joergensen, P. S., . . . Levin, S. M. (2018). A new model of jupiter’s magnetic field

293

from juno’s first nine orbits. *Geophysical Research Letters*, *45*(6), 2590–2596. doi:

294

10.1002/2018GL077312

295

Connerney, J. E. P., Timmins, S., Oliverson, R. J., Espley, J. R., Joergensen, J. L.,

296

Kotsiaros, S., . . . Levin, S. M. (2022). A new model of jupiter’s magnetic field at

297

the completion of juno’s prime mission. *Journal of Geophysical Research-planets*,

298

*127*(2), e2021JE007055. doi: 10.1029/2021JE007055

299

Karniadakis, G. E., Kevrekidis, I. G., Lu, L., Perdikaris, P., Wang, S., & Yang,

300

L. (2021). Physics-informed machine learning. *Nature Reviews Physics*, *3*(6),

301

422–440.

302

Kaspi, Y., Galanti, E., Hubbard, W. B., Stevenson, D., Bolton, S., Iess, L., . . . oth-

303

ers (2018). Jupiter’s atmospheric jet streams extend thousands of kilometres deep.

304

*Nature*, *555*(7695), 223–226.

305

Kingma, D. P., & Ba, J. (2015). *Adam: A method for stochastic optimization*. Re-

306

trieved from <http://arxiv.org/abs/1412.6980>

307

Lowes, F. (1974). Spatial power spectrum of the main geomagnetic field, and extrap-

308

olation to the core. *Geophysical Journal International*, *36*(3), 717–730.

309

Lu, L., Meng, X. H., Mao, Z. P., & Karniadakis, G. E. (2021). Deepxde: A deep

310

learning library for solving differential equations. *Siam Review*, *63*(1), 208–228.

311

doi: 10.1137/19M1274067

312

Mauersberger, P. (1956). Das mittel der energiedichte des geomagnetischen haupt-

313

feldes an der erdoberfläche und seine saulare anderung. *Gerlands Beitr. Geophys.*,

314

*65*, 207–215.

315

Moore, K. M., Cao, H., Bloxham, J., Stevenson, D., Connerney, J., & Bolton, S.

316

(2019). Time variation of jupiter’s internal magnetic field consistent with zonal

- 317 wind advection. *Nature Astronomy*, 3(8), 730–735.
- 318 Moore, K. M., Yadav, R. K., Kulowski, L., Cao, H., Bloxham, J., Connerney, J. E.,  
319 ... others (2018). A complex dynamo inferred from the hemispheric dichotomy of  
320 jupiter’s magnetic field. *Nature*, 561(7721), 76–78.
- 321 Nabian, M. A., Gladstone, R. J., & Meidani, H. (2021). Efficient training  
322 of physics-informed neural networks via importance sampling. *Computer-  
323 Aided Civil and Infrastructure Engineering*, 36(8), 962–977. Retrieved from  
324 <https://onlinelibrary.wiley.com/doi/abs/10.1111/mice.12685> doi:  
325 <https://doi.org/10.1111/mice.12685>
- 326 Raissi, M., Perdikaris, P., & Karniadakis, G. E. (2019). Physics-informed neural  
327 networks: A deep learning framework for solving forward and inverse problems in-  
328 volving nonlinear partial differential equations. *Journal of Computational Physics*,  
329 378, 686–707. doi: 10.1016/j.jcp.2018.10.045
- 330 Ridley, V. A., & Holme, R. (2016). Modeling the jovian magnetic field and its sec-  
331 ular variation using all available magnetic field observations. *J. Geophys. Res.:  
332 Planets*, 121(3), 309–337.
- 333 Sharan, S., Langlais, B., Amit, H., Thebault, E., Pinceloup, M., & Verhoeven,  
334 O. (2022). The internal structure and dynamics of jupiter unveiled by a high-  
335 resolution magnetic field and secular variation model. *Geophys. Res. Lett.*, 49(15),  
336 e2022GL098839.
- 337 Wang, S. F., Teng, Y. J., & Perdikaris, P. (2021). Understanding and mitigating  
338 gradient flow pathologies in physics-informed neural networks. *Siam Journal on  
339 Scientific Computing*, 43(5), A3055–A3081. doi: 10.1137/20M1318043
- 340 Wu, C. X., Zhu, M., Tan, Q. Y., Kartha, Y., & Lu, L. (2023). A comprehensive  
341 study of non-adaptive and residual-based adaptive sampling for physics-informed  
342 neural networks. *Computer Methods in Applied Mechanics and Engineering*, 403,  
343 115671. doi: 10.1016/j.cma.2022.115671